

## Flexural Models for Vacuum-Packed Particles as a Variable-Stiffness Mechanism in Smart Structures

J. David Brigido<sup>1,\*</sup>, Steve G. Burrow,<sup>1</sup> Benjamin K.S. Woods,<sup>1</sup> Piotr Bartkowski<sup>2,†</sup> and Robert Zalewski<sup>2</sup>  
(Bristol-Warsaw Collaboration)

<sup>1</sup>University of Bristol, Queen's Building—University Walk, Bristol BS8 1TR, United Kingdom

<sup>2</sup>Warsaw University of Technology, Narbutta 84, Warsaw 02-524, Poland

 (Received 1 February 2021; revised 23 June 2021; accepted 4 March 2022; published 11 April 2022)

Vacuum-packed particle (VPP) systems have been recently used in the development of smart structures due to their ability to actively change material stiffness through the mechanism of granular jamming. By altering the strength of the vacuum pressure applied to the particles, the material can be proportionally and reversibly transitioned from a liquidlike low-stiffness state to a stiff state. The ability to control material stiffness in this way opens up different possibilities for the design of morphing and smart structures by allowing them to soften during deformation to reduce actuation energy requirements and to then stiffen once the desired shape has been achieved to provide a zero-energy holding mechanism. The following research describes two useful models that predict the mechanical response of VPP beams under flexural loading. Firstly, four-point bending tests with digital image correlation strain mapping are performed in order to measure the axial and transverse strains in a bending beam made from vacuum-packed particles. The test results show a nonlinear mechanical response, including a change in beam thickness with deformation, that motivated an analytical model of the structure incorporating a nonlinear material stress model based on the Mohr-Coulomb failure envelope. In addition, finite-element simulations are implemented using a Johnson-Cook model extension to predict the response under loading of three-dimensional beam elements at different vacuum pressure levels. Lastly, the models are compared to the experimental results, indicating good agreement. Both methods are shown to be useful for predicting the variation of stiffness of vacuum-packed particle beams.

DOI: [10.1103/PhysRevApplied.17.044018](https://doi.org/10.1103/PhysRevApplied.17.044018)

### I. INTRODUCTION

Vacuum-packed particle (VPP) structures are made of a large number of discrete material grains (e.g., glass beads, sand, ground coffee, etc.) held within a sealed elastic membrane [1,2]. The overall structural stiffness can be reversibly changed from liquidlike to solidlike by removing the air from within the membrane with a vacuum pump. The confining pressure created by the vacuum compresses the grains together, mechanically locking them into a solid structure in a phenomenon known as granular jamming [3]. The number of grain-to-grain contacts and the grain shear properties significantly impact the overall effective stiffness of the bulk structure, with a further dependence on the magnitude of the confining pressure.

In recent years, granular-jamming structures have been used to build various concepts of smart structures to vary their stiffness depending on operating conditions. One

smart structure that used vacuum-packed particles was Petrovic's smart dome [4]. The dome has polystyrene beads inside a polymer membrane and can be reshaped into different geometries. Granular jamming has also been applied in the field of soft robotics, particularly for bending-dominated applications. Cheng *et al.* developed a granular robotic arm for gripping delicate objects [5]. The soft robotic manipulator consists of several parts that can be actuated into various positions using internal tensioned cables. The performance of the arm is enhanced by incorporating granular jamming. The robot can locally change the stiffness of each section during deformation without affecting the overall control of the desired position, allowing the driving actuators' size and power requirements to be reduced to achieve a specified stiffness under load. The most common application and commercialization of robots using VPP is the universal robotic grip proposed by Brown *et al.* [6]. The robot can smoothly adapt its shape to grab fragile objects like eggs, fruits, etc. Surgical endoscope and catheter devices have also been developed and tested with granular jamming in order to provide variable stiffness instruments for improved patient care [7,8].

\*david.brigido@bristol.ac.uk

†piotr.bartkowski@pw.edu.pl

The present authors have been developing a morphing aerostructure using vacuum-packed particles to switch the stiffness of a wing at different flying conditions [9]. The morphing system is the fish bone active camber (FishBAC) concept [10] modified with the addition of vacuum-packed particles. FishBAC is an actuated compliant trailing edge that bends to actively control airfoil camber and therefore lift generation. FishBAC achieves changes in lift with significantly less drag penalty than traditional aircraft control surfaces (trailing edge flaps), as shown in recent wind-tunnel tests [11]. The morphing trailing edge consists of a collection of stringers attached to a flexible spine to define the airfoil shape. The spine is a continuous, compliant structure that smoothly deflects the trailing edge. In this work, the spaces between adjacent stringers are filled with granular media (which is ground coffee in the initial experiments), and by turning on and off the vacuum, the bending stiffness of the spine can be controlled. The morphing concept is morphed with the vacuum off to minimize energy requirements. Once the desired shape is achieved, the vacuum pressure is applied to stiffen the device—providing increased resistance to external load fluctuations and providing a zero-energy shape hold. Ground coffee is used in this initial work because it is light in weight and rough in shape, with the roughness creating mechanical interlocking, increasing strength. It is envisioned that higher-performance engineered materials would be used in real-world applications.

Bending properties are a critical aspect for smart structures, as achieving good bending stiffness and strength is a key design requirement for many of the morphing concepts proposed to date. Recent work has focused on the bending properties of granular media systems. Bartkowski *et al.* [12], Brigido *et al.* [9], and Huijben *et al.* [13] have undertaken flexural testing of rectangular beams made from vacuum-packed particles. Bartkowski suggested three-point bending testing to obtain the nonlinear stress-strain curves of polyoxymethylene-sphere samples inside a polyethylene membrane. On the other hand, Huijben and Brigido both used four-point bending to quantify the flexural stiffness of different granular materials.

The most common materials used for vacuum-packed particle testing and applications are glass beads, styrofoam balls, ground coffee, seeds, sand, plastic pellets, wooden sticks, etc. [8,14–18]. The materials according to various shapes and sizes, were analyzed in triaxial compression and flexural tests [13,18,19]. The researchers also analyzed several membranes, including flexible and rigid polymers [13,15]. The experiment's findings revealed the following trends:

(a) Granular-jamming devices composed of rough surface particles (also known as frictional materials in the literature) are substantially stiffer than other VPP structures composed of smooth surface particles (frictionless

materials). Triaxial compression tests have reported a direct correlation between the internal frictional angle and the structure's overall stiffness and strength. Frictional particles exhibit greater internal friction angles than frictionless particles, furthermore a greater stiffness and strength.

(b) Shape influence has been studied in the definition of circularity or sphericity, and researchers have been trying to find whether there is some relationship between internal friction angle and circularity. The overall stiffness of the structures has a shape dependence described by the following power law  $E = (\sigma_c)^n$ .  $E$  represents the stiffness,  $\sigma_c$  is the confining pressure, and the exponent  $n$  is the shape dependence, which is parameterized by the particle circularity. However, the shape dependence is dependent on contact forms, and the power-law shape condition does not work on certain materials. For example, glass-bead spheres are well known to create Hertzian contact interaction among particles. In contrast, nonspheres' shape particles can change drastically in many contact areas depending on interlocking effects (e.g., surface roughness).

(c) The size distribution has been analyzed in terms of polydispersity for some materials. The testing results suggest that nonuniform collections (a combination of large and small particles) present higher stiffness and strength than uniform-collections (same size particles). Nonuniform collections can fill cavities where only small particles can fit and increase the number of contacts by entangling with large particles. Nevertheless, the size distribution may not influence some materials' overall stiffness. The use of various nonuniform collections of sand and ground coffee (e.g., coarse and fine grain) do not result in any noticeable reduction or increase in their stiffness. In contrast, glass beads can increase their packing fraction and stiffness by having an optimal nonuniform collection.

(d) The influence of membrane stiffness is rather limited in VPP structures for membranes with a lower elastic modulus than the particle's bulk stiffness. However, it can significantly change the softening-stiffness region and hysteresis by using stiffer membranes.

(e) The tuning of the particle properties (e.g., size, shape, etc.) can switch the overall stiffness of VPP structures up to 50% depending on the material. Nonetheless, the best way to adjust the structure's stiffness is by deliberately raising or decreasing the confining pressure, which can be actively controlled by vacuum actuators. Depending on the vacuum stage, the flexural stiffness can switch up to more than 200%.

All the above-mentioned flexural procedures generally have similar trends to their load-displacement curves for loading and unloading cases (see Fig. 1). Overall, the behavior is highly nonlinear. There is a roughly linear region of the response under initial loading. Huijben explained that the core of the beam or granular media

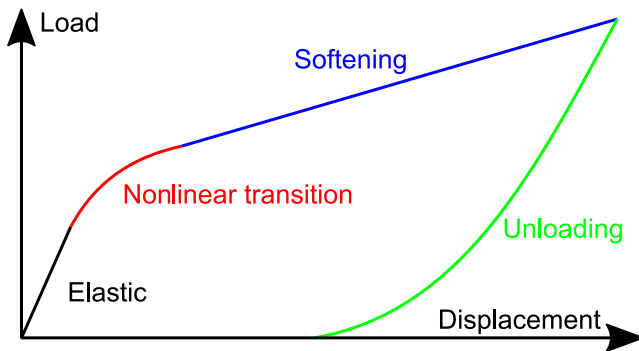


FIG. 1. Load-displacement curves of vacuum-packed particle beam testing [9,12,13].

works entirely in compression due to hydrostatic pressure. Most of their linear behavior is influenced by the shear stiffness of the grain [16]. Then, as the displacement increases, a nonlinear stiffness-softening emerges from the grain rotational and translational kinematics. In this region, the locking forces (friction and force chains) cannot hold static equilibrium based on the overall number of contacts for a packing fraction condition controlled by confining pressure; therefore, the particles move relative to each other, increasing the number of floating particles (particles that are split away from the interconnected force chains). During an unloading event, there will be a notable presence of hysteresis regardless of strain rate [15].

Several attempts to model the complex nonlinear behavior of these materials have been proposed. Huijben *et al.* proposed a discrete-element method (DEM) to capture the softening region by examining the force chains' distribution throughout the particles. On the other hand, Brigido *et al.* modeled this nonlinearity based upon the von Mises plasticity model within a nonlinear finite element analysis (FEA) analysis, with the relevant material properties being determined from experimental stress-strain curves. Bartowski *et al.* also used a plasticity approach based on a modified form of the Johnson-Cook model by adding a material parameter, which describes the amount of confining pressure extent in the structure [9]. These methods all require experimentally determined stress-strain relationships for a given granular material, at a range of different pressures, in order to model the material response. Even with experimentally determined material behavior, the highly nonlinear behavior of any given structure made from the material can still be difficult to predict accurately using these models. The response of the structure is driven by a complex interaction between the bending mechanics at the structural level and the complex load carrying and failure mechanisms of the granular media. This motivates further study of the flexural response of granular media, which combines carefully designed and highly instrumented experimental testing alongside further consideration of modeling methods.

The following research does not attempt to analyze the microinteractions between grains such as force chains, which is a highly complex kinematic analysis with many degrees of freedom and design variables [20–24]; rather, discrete analyses such as the Lubachevsky-Stillinger algorithm and the discrete element methods mentioned before, are best suited for this purpose. For small-scale applications, especially when the volume of particles is low, these discrete methods can capture the response at a reasonable level of computational cost [25,26]. However, we are interested in larger-scale smart structures that can vary stiffness by controlling the hydrostatic stress (confining pressure) in the grains. Due to the size of these structures, many thousands or even millions of individual particles will be present. Attempting to model each and every one of these particles using the discrete methods will very quickly result in very computationally expensive problems. For initial design space explorations or design optimization, this cost will be prohibitive and will severely limit the number of configurations that can be considered. Furthermore, many types of smart structures are composed not only of granular materials but also of solid continuum isotropic and anisotropic materials such as plastics or composite materials like carbon fiber and epoxy matrix, which are better analyzed using continuum mechanics approaches. The physics underlying the stiffness mismatch between the interaction of grains and the solid continuum materials may require a hybrid analysis between discrete and continuum methods like integrated DEM-FEM approaches. Combining DEM's microscale elements with macroscale finite-element methods increases even further still the complexity and computational cost of the analysis. Work integrating DEM-FEM approaches is present in the literature, with one example structural analysis based on thousands of individual particles taking many days to compute, even with parallel programming and powerful computer hardware [27]. However, for applications involving millions of particles and complex geometries, this type of analysis discourages and increases the expense of designing smart structures with vacuum-packed particles, particularly when the analysis is conducted under a range of hydrostatic stress conditions and external loading.

In contrast to relatively costly DEM models, soil continuum mechanics models are commonly employed in the development of various flexural applications [28–31]. The majority of continuum models for soils are based on critical state theory [32–34], in which failure and plastic deformations are represented by a variety of distinct constitutive models, such as the modified Cam-Clay or Johnson-Cook models [35,36]. Several of these models use Mohr-Coulomb or Matsuoka-Nakai failure criterion-governed failure surfaces [37], which reduce the complicated interactions of the granular assembly into a simple idealization of stress states capable of capturing certain mechanical

properties such as strength or stiffness. State-of-the-art continuum models have expanded their constitutive framework by integrating anisotropy and dilatancy state lines into the critical state theory [38–40]. Anisotropy is incorporated into these models primarily via the use of a fabric tensor [41], which enables the description of randomly packed granular structures using the concept of a void cell system, which characterizes the form and direction of the voids inside the granular assemble [42]. On the other hand, dilatancy is introduced into the critical state theory to measure the shear-induced volume change of the whole aggregate [43]. The fabric tensor and load-carrying direction are combined to define dilatancy state lines, from which a state parameter called the dilatancy state parameter is derived to quantify the void cell system’s contracting and dilation strain trends [38,44]. These strain trends have been studied in a variety of anisotropic critical state theory models [45], with the results indicating that dilatancy is significantly impacted by the direction of the load, with the stress and volume change being analyzed in principal stress trajectories [46,47].

This research aims to take a different approach than the described models above, one that is far more straightforward and computationally efficient. The proposed models derive a continuum mechanics approach for a volume of particles, idealizing complicated microscopic grain interactions by leveraging existing macromechanical models from the field of soil mechanics [48–55]. The volume is assumed to be large enough to accommodate a large number of particles, allowing macroscopic variables such as bulk stiffness under various hydrostatic stress conditions to be effectively captured. These continuum models minimize the number of design variables, which can be advantageous in developing smart structures.

The following study explores the mechanical response of vacuum-packed, ground coffee filled beams in more detail than the previous work done by the authors [9] through improved measurement techniques, including the use of digital image correlation to create full-field strain maps and pressure sensors to accurately measure the vacuum pressure within the beam itself. Measurements of through-thickness strains are isolated from the full-field measurements and recorded at different levels of vacuum pressure. These measurements are particularly useful for investigating particle motion in the softening region. An analysis method based on the inclusion of a Mohr-Columb failure envelope criteria within a modified Euler beam theory is introduced to capture the softening nonlinearity. In parallel, finite-element analysis of the same structure using an extension of Johnson-Cook model, implemented into the commercial FE code LS-DYNA, is used to analyze the stiffness response of VPP beams. Finally, both models are compared, and their relative merits, shortcomings, and drawbacks within the context of vacuum-packed particle-based smart structures are discussed.

## II. FLEXURAL TESTING OF VACUUM-PACKED PARTICLE BEAMS

### A. Flexural testing with video gauge system

While a range of materials have been investigated in previous work, this paper focuses on coffee grinds as the granular media, as they have a high stiffness-to-weight ratio, which is of course paramount for aerospace applications. While perhaps not a desirable material for real-world application, coffee grinds are a useful “placeholder” material as more robust engineered material alternatives are sought.

In order to measure the flexural stiffness of granular-jamming beams, a series of four-point bending tests are performed. Three rectangular VPP beams with a cross section of 120 mm by 40 mm and a length of 580 mm are manufactured, with the beams being identical except for skin thickness. Three thicknesses (0.25, 0.5, and 0.8 mm) of the silicone skin sheets (Silex SuperClear [56]) are tested to investigate the impact of skin stiffness. The specimens are prepared (see Fig. 2) as follows. Two cuboid end fittings are manufactured from a three-dimensional (3D) printer filament (Polylactic acid) to maintain the beam’s rectangular cross-section shape. Three holes pierce the end fittings to allow the content to get in and attach the vacuum sensors (model PSE53 from SMC [57]).

A female mould made of MDF wood with the beam’s shape is used to ensure continuity and repeatability. The membrane is placed within the wooden mould; then, rigid end fittings are placed at each end of the beam to set the cross-section form. A rectangular cross-section shape foam beam with the beam’s dimensions is positioned next to the

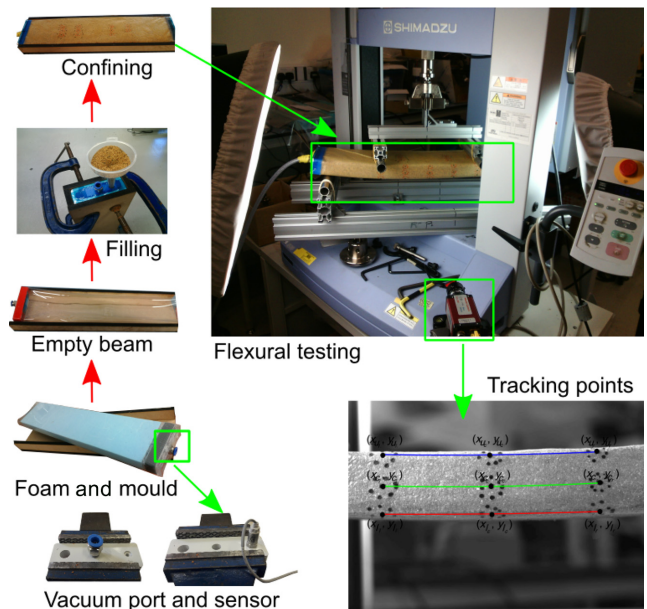


FIG. 2. VPP beam preparation and flexural test setup.

end fittings. The membrane wraps the foam outline, and one of the end fittings is glued to the membrane using silicone adhesive. The foam is removed from the skin, and the remaining end tap is glued to seal the beam. Then, the membrane is placed inside the mould, clamped on the outside, and placed vertically with one of the end taps facing upwards. Therefore, a funnel is filled with ground coffee through one of the openings. The sample beam’s mass is determined using a calibrated scale. The beam retains its rectangular cross-section shape over the span by having a confining pressure above 2 kPa. The vacuum pump can change the vacuum level from 0.01 to 0.99 Bar. Upon achieving the desired pressure, the box is then disassembled, and the requested sample extracted.

A video extensometer (iMETRUM, Allied Vision Manta G-504 B/C GigE Camera 2452 3 2056) is used to capture beam displacements at multiple tracking points. The tracking points are drawn at three different locations to plot three lines along the span. One line is positioned at the top of the beam (see the blue line on Fig. 2) to measure the compression strain. Another line is at the bottom to measure the tensile strain (red line). The remaining line (green) is positioned at midheight to see if there are sudden shifts on the membrane deformation.

The four-point test rig is determined in accordance with ASTM Standard C880/C880M. The load cycle is applied at a strain rate of 10 mm/min through two rollers (diameter of 22 mm) gripped to the test frame machine’s load cell. The test runs until the gripper rollers exceed a length of 90 cm; then, the load is held for 5 s. Eventually, the beam is unloaded after.

In addition to the three membrane thicknesses (0.25, 0.5, 0.8 mm), four different vacuum pressure levels (23, 52, 75, 91 KPa) are tested. Eight repeated tests are run for each combination of skin thickness and pressure, leading to a total of 32 tests for each thickness and 96 tests overall. Table I shows the weight, vacuum level, membrane thickness, and the number of tests conducted on each of the beams.

Figures 3 and 4 display the load-displacement and moment-curvature graphs from the testing results. It can be seen that while the overall response of the structures is highly nonlinear, there is an initial portion of the response that is roughly linear, after which a softening nonlinearity begins. Given the known geometry of the beams, an equivalent flexural modulus can be derived from the load

TABLE I. Beam samples for flexural testing.

Type	Weight (Kg)	Skin (mm)	Vacuum (kPa)	Tests (no.)
S25	1.00	0.25	23 – 91	8 × 4 = 32
S50	1.01	0.50	23 – 91	8 × 4 = 32
S80	1.02	0.80	23 – 91	8 × 4 = 32

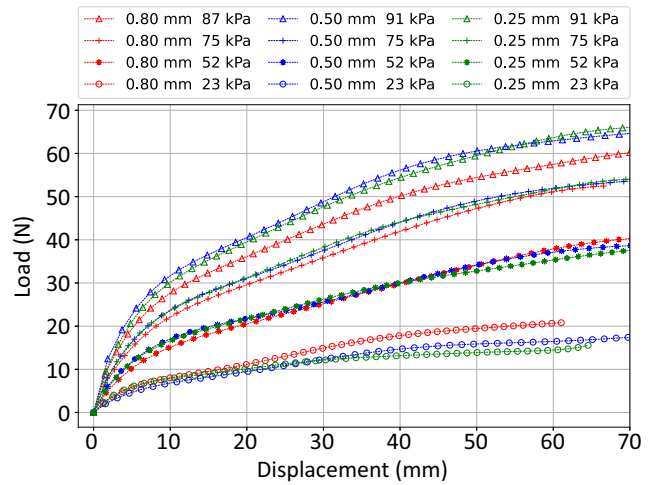


FIG. 3. Load-displacement curves for the flexural tests.

displacement curved. This is done both for the initial linear region and for the large displacement plastic region of the responses, as shown in Fig. 1. Table II lists these calculated rigidity values for the different pressure tested. Furthermore, the test results indicate that there is no difference when adjusting the thickness of the membrane, meaning that the overall stiffness of the system is completely influenced by the stiffness of the grain.

**B. Flexural testing with digital image correlation**

Notably, the previous results show the nonlinear stiffness measured at the loading points. The full response of the structure is of course considerably more complex, with strain and stress variations expected along all three dimensions of the beam’s geometry. While measuring the fully three-dimensional response of a structure made from granular media is an incredibly challenging task, significant insight can be gained by considering the

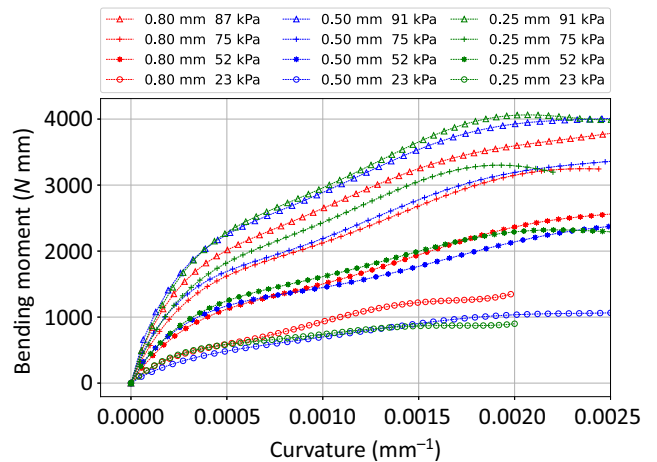


FIG. 4. Moment-curvature plots for the flexural tests.

TABLE II. Initial  $EI_i$  and plastic  $EI_p$  stiffness for each sample at various vacuum pressure.

Vacuum (kPa)	$EI_i$ (MPa)	$EI_p$ (MPa)
23	$16 \times 10^5$	$47 \times 10^4$
52	$32 \times 10^5$	$73 \times 10^4$
75	$48 \times 10^5$	$106 \times 10^4$
91	$68 \times 10^5$	$133 \times 10^4$

response to be constant along the width of the beam [two-dimensional (2D) beam assumption] and using digital-image-correlation (DIC) techniques to measure the strains in the height-length plane, which is visible at the side of the beam. The primary objective of the flexural tests using DIC is not to characterize the micromechanical properties of the granular media but instead to determine the deformation characteristics of the beam during bending and, implicitly, to determine whether dilation occurs as a result of grain motion. A further complication comes from the presence of the skin membrane, which complicates tracking of the granular media directly. The skin used here is very soft and thin, and is held in direct contact with the grains by the vacuum pressure and so it is reasonable to assume that it deforms along with the particles, at least for moderate strains.

As seen in Fig. 5, a 5-MP CCD camera manufactured by LaVision is oriented perpendicular to the beam’s length axis at a distance of 70 cm in order to capture strains in the height-length plane within a capture area of 125 by 39 mm centered on the midspan location. This measurement window is chosen as the best compromise between resolution and measurement area for the given camera system. Note that this window is fully within the two central loading rollers, and so is in the constant bending moment portion of the beam when loaded. Additional lighting is provided by two high-intensity white light-emitting diodes (LEDs) mounted at  $\pm 45^\circ$  relative to the camera’s sensor plane. Polarized lens filters are used to help filter out other light sources in the lab, minimizing reflections.

We follow “The art and application of DIC” by Philip Reu [58] to perform the best practices and minimize errors caused by lens warping, lighting, speckle pattern, magnification, etc. Although calibration is not required in 2D DIC, it is a standard procedure in most LaVision DIC systems to minimize lens warping error. Long focal length lenses are used to minimize the radial lens distortions; also, the viewing through optical surfaces is corrected with appropriate calibration. Table III details the number and type of sensors and lenses. Calibration plates are used to correct lens distortions and ensure proper image scaling. The calibration procedure is accomplished by performing a series of calibration motions defined by grid fills on plates, this procedure is carried out using the LaVision procedure manual guide. The calibration target should be rotated,

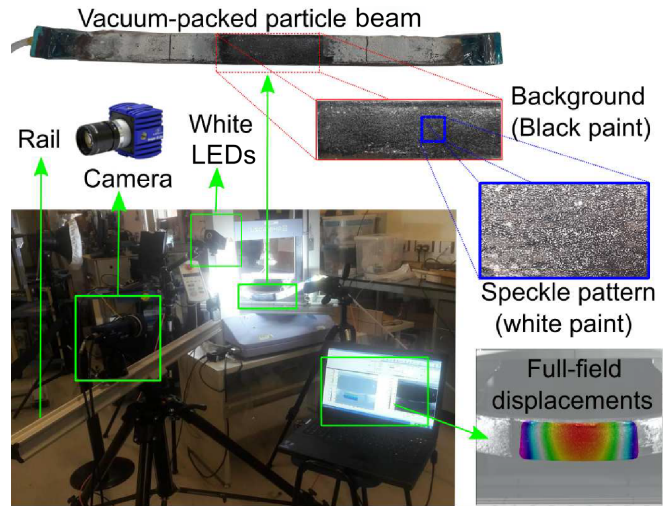


FIG. 5. Flexural test setup and speckle pattern for DIC.

tilted, and translated across the entire field of view while taking images throughout the process. The LaVision DIC software determines the number of images and prescribed motions. Also, during the calibration process, the magnification factor and focal length are adjusted with a rail (see Fig. 5) to control the depth of field and, therefore, the corresponding dimension on the image plane camera.

Ensuring a good calibration procedure is critical to keep most of the uncertain error on the speckle pattern, which is intrinsically related to the spatial resolution of the images. According to the sampling theorem, the minimum distance required to determine accurate measurements is a  $2 \times 2$  pixel pattern sample (black and white contrast). In practice, a speckle of  $3 \times 3$  pixels is the smallest size that prevents aliasing. The DIC technique requires a stable,

TABLE III. Data analysis and filtering parameters for DIC.

Technique used	2D digital image correlation
Sensor and digitalization	Imager X-lite 5 Mpixel
Camera noise (% range)	0.7%
Lens and imaging distance	Tokina AT-X M100 ProD, 70 cm
Image recording frequency	1 Hz
Pixel to mm conversion	1 pixel = 0.0055 mm
Field of view	125 mm $\times$ 39 mm
Subset, step	$25 \times 25$ pixel, 8 pixel
Interpolation	Cubic spline
Shape functions	affine
Correlation criterion	ZNSSD
Presmoothing	Gaussian 5
Spatial resolution	0.3682 mm
Smoothing technique	Local polynomial—affine
Strain window	9 data points
VSG	81 pixels, 6.89 mm
Resolution	$2.3 \times 10^{-4}$

high-contrast speckle pattern to recreate a strain field accurately. This is not a trivial consideration given the clarity and poor adhesive properties of the silicone skin, but a viable solution is found through experimentation, which uses two layers of water-based paints with additives to ensure adhesion to the silicone. A layer of black paint is first applied as a background, and then white paint is applied with a sponge roller to create a speckle pattern. We observe that the minimum number of pixels required to process images within a given field of view correctly is greater than the grain pixel size and that a cell size of  $25 \times 25$  is the optimal pixel window size for obtaining the highest spatial resolution with the lowest possible noise. At least 12 speckles per subset on a speckle radius of 5 pixels are painted. Figure 5 shows the speckle pattern for DIC testing.

The construction of DIC algorithms, interpolation, shape function, matching, and correlation are performed using the LaVision software setup (DaVis 8.3.1), which is capable of filtering and postprocessing displacement data, as well as strain calculation from displacements given the input parameters shown in Table III. Due to limited availability of the camera system, DIC results are only taken for the beam with 0.5-mm-thick skin (S50) at vacuum

pressures of 52, 75, and 91 kPa. Nonetheless, we validate the DIC test’s accuracy by comparing it to video gauge tests. The video gauge system test tracks only a single point during deformation, on the other hand, a single point from the DIC’s entire field deformation can be subtracted and compared to the video gauge data. Both results demonstrate comparable strain deformation with a relative error of less than 10%.

Figures 6 and 7 show an example of the DIC results for the VPP beam with 0.5-mm skin thickness (S50) at 91-KPa vacuum pressure and a displacement of 70 mm. Here we see significant variance in strain through the height of the beam, and a more modest amount of variance along its length. Figure 6 displays the variance of axial strain through the height of the beam, at the center of its span. It can be seen that the axial strain varies in a roughly linear manner with height, which is also seen at other length positions, displacements, and pressures. However, the neutral axis is moved upwards as the vacuum pressure decreases. Unlike low-vacuum levels, the neutral axis appears to go down, with high-pressure levels.

Figure 7 presents the transverse strains (that is strains in the height direction) at the beam’s middle span section. The transverse strain distribution reveals a nonlinear trend,

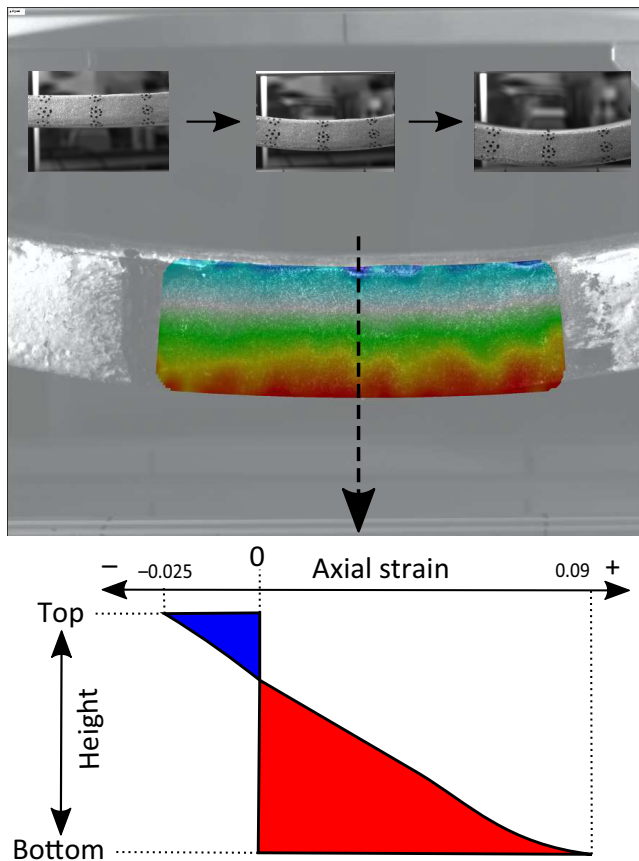


FIG. 6. Full-field axial strains.

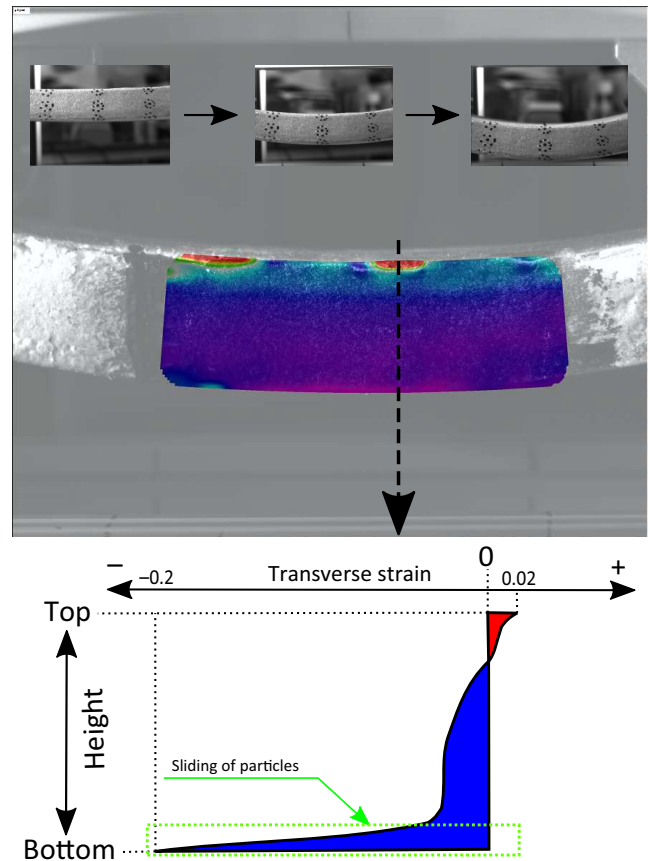


FIG. 7. Full-field transverse strains.

especially at the beam’s bottom edge. The nonlinear pattern implies grain motion that thins the cross-section area. Particles on the bottom section split from the middle to the sides as the bending moment increases. Observing this nonlinear behavior suggests the following hypothesis: the bottom grains cannot endure tensile stress as the bending moment increases. Tensile stresses cause the grains to split away from each other and then coalesce with grains from other strata under the vacuum pressure, reducing the cross-section height. The preceding assumption encourages a stress-distribution state that can only sustain compression stress and is limited to reducing the second moment of area as the bending moment increases.

### III. ANALYTICAL VACUUM-PACKED PARTICLE-BEAM MODEL INCLUDING SHEAR FAILURE

#### A. Introduction and motivation of the model

In this section an analytical model of vacuum-packed particle-beam (VPPB) structures is developed, which incorporates methods from beam theory, inflatable structures, and soil mechanics, in a manner that is informed by the behavior seen in the nonlinear full-field strain distribution on the beam’s wall side. We start with the assumption that although the details of the grain contacts and interactions at the microscale are extremely complex, at the macrolevel the behavior of the grains can be captured by considering grain-shear-failure effects and beam thinning. The thinning is attributed to grain dilatation and has also been seen in triaxial compression tests under a variety of hydrostatic conditions. This dilation is modeled as a grain-failure condition due to the grain’s inability to withstand tensile stress.

This inability to withstand tensile stress motivates a comparison to inflatable structures [59]. Inflatables structures are often made from flexible fabric materials, which on their own cannot withstand any compressive stresses, as they have very low buckling strength [60]. What gives inflatable structures the ability to carry bending loads (which of course induce compression in portions of the structure) is the tensile bias stress created in the fabric by the internal pressurization. The strength of an inflatable structure is in large part determined by this bias stress, as increasing load will eventually lead to the compressive bending stresses overcoming this bias stress to create a local condition of net compressive stress, which will cause local buckling of a portion of the beam, reducing its stiffness progressively as load increases.

In a similar, albeit reversed, fashion the granular media are not able to withstand tensile stresses, as the grains will simply pull away from each other. VPP beams are able to carry bending loads (which do include tensile stresses) because a compressive bias stress is created by the vacuum pressure, and so long as this bias stress is larger

than the local stresses induced by bending, that portion of the beam is able to carry load. The failure mechanism can be conveniently implemented into the beam model by assuming a linear zero-stress state condition that transforms the second moment of area into a cubic function with decremental variation as the bending moment increases. The zero-stress state condition has been used to model the softening stiffness region in various beam applications, including inflatable beams that buckle in compression. In addition, prestress concrete beams are analyzed similarly because the crack propagation results in a zero-stress condition when the concrete cannot resist tensile stress [61–64]. The beam model proposed in this research considers this zero-stress state condition under various hydrostatic stress conditions using the Mohr-Coulomb failure criteria [65], which can easily analyze the grains’ mechanics and reduce the number of design variables. Borrowed from soil mechanics, with soils of course being a form of granular media, the Mohr-Coulomb failure criteria represents and idealizes all the micromechanic variables such as packing fraction, grain size, surface roughness, type and number of contacts, etc., by accounting only for the packing fraction angle and cohesion parameters at various hydrostatic stress conditions.

#### B. Dilatancy and effective stress

Soil structures usually change volume if sheared—a phenomenon known as dilatancy [66–68]. In other words, the grain structure either expands or shrinks through shear deformation. Figure 8(a) displays two layers of loose particles, which are sheared by a misalignment of two axial forces. If soil structures are subjected to bending loads, the grains pull away in different directions. As the bending moment increases, the sheared deformation of the lowest layer of the beam will pull the grains away from the middle section, forcing the cross-section area to decrease. This phenomenon is known as the splitting condition and is seen

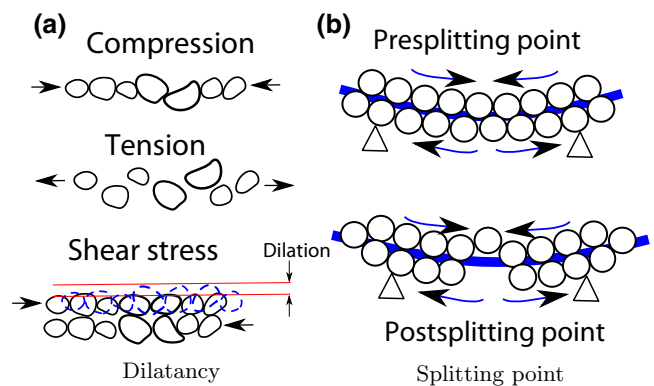


FIG. 8. Dilatancy on grains due to shear stress (a) and the splitting point due to bending moment (b).

in Fig. 8(b). The DIC findings from Sec. II suggest that the nonlinear behavior may emerge by this splitting condition.

Vacuum-packed particle structures are internally saturated with vacuum pressure. The pressure exerted by the vacuum is defined by the hydrostatic stress tensor, which is the average of the three normal stresses, and is given by the following set of equations:

$$\sigma_{\text{hyd}} = \frac{\sigma_{11} + \sigma_{22} + \sigma_{33}}{3}, \quad (1a)$$

$$\sigma_{\text{hyd}} = \frac{1}{3} \text{tr}(\boldsymbol{\sigma}) = \frac{1}{3} I_1 = \frac{1}{3} \sigma_{kk}, \quad (1b)$$

where  $\sigma_{\text{hyd}}$  is the hydrostatic stress,  $\sigma_{11}$ ,  $\sigma_{22}$ ,  $\sigma_{33}$ , are the normal stresses of the identity matrix  $\text{tr}(\boldsymbol{\sigma})$ . If the hydrostatic term is removed from the stress tensor, the remaining term is known as the deviatoric stress.

$$\mathbf{S} = \boldsymbol{\sigma} - \sigma_{\text{hyd}}, \quad (2a)$$

$$S_{ij} = \sigma_{ij} - \frac{1}{3} \delta_{ij} \sigma_{kk}, \quad (2b)$$

The stress tensor under hydrostatic pressure can be decomposed into the deviatoric and the hydrostatic part

$$P = -\frac{1}{3} \sigma_{kk}. \quad (3)$$

The equilibrium forces inside the VPP structure are equal to the external forces. Therefore, the particles are fully saturated with some vacuum pressure acting between the external forces and the contact forces of the grains [see Fig. 9(a)]. The total stress in the vacuum-packed structure is represented in the following equation:

$$\boldsymbol{\sigma} = \boldsymbol{\sigma}_n - P. \quad (4)$$

Equation (4) introduces an effective stress term  $\boldsymbol{\sigma}_n$ , which is the stress that holds the particles together. When

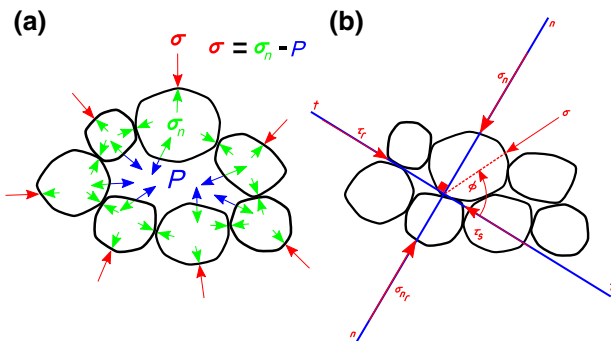


FIG. 9. Effective (a) and shear stress (b) for vacuum-packed particles.

the external stress is greater than the effective stress, the particles will split away, and dilatancy occurs. In some way, this concept describes the failure mechanism of the bulk structure when the shear strength cannot resist the deformation by tangential stress known as well as the shear stress  $\tau_s$ . The shear strength equation can be derived from Fig. 9(b) and is shown in the next equation:

$$\tau_s = \sigma_n \tan \phi + C. \quad (5)$$

Equation (5) is known as the Mohr-Columb failure envelope. It describes the shear stress  $\tau_s$  as a function of the normal effective stress  $\sigma_n$ . The shear strength is calculated as the maximum shear stress  $\tau_{\text{max}}$  that the granular structure can resist through frictional and intermolecular forces. This first term relates the resistance to displacement due to interlocking and internal friction. The interlocking effect is driven by the shape and size of the particles, and the intensity of the interlocking can substantially increase by increasing the packing fraction. The interlocking resistance is smaller for flat and symmetric shaped particles (e.g., spheres, squares, etc.). In contrast, the interlocking resistance is higher by having a mixture of various shapes. On the other hand, the frictional resistance describes the opposition of the relative motion of two or more particles in contact. The coefficient of friction characterizes the magnitude of this resistance in a kinetic  $f_s$  and static  $f_k$  manner. The kinetic coefficient  $f_k$ , also known as the sliding friction, is determined by the tangential force  $T_k$  required to sustain a steady motion of two surfaces in close contact, which are held together by a normal force  $N$  using the following relation:

$$f_k = \frac{T_k}{N}. \quad (6)$$

In comparison, the coefficient of static friction  $f_s$  is described by the shear strength required  $\tau_{\text{max}}$  to cause relative motion by holding together both surfaces in contact with the normal stress:

$$f_s = \frac{\tau_{\text{max}}}{\sigma_n}. \quad (7)$$

Usually, the coefficient of static friction is larger than the sliding friction  $f_s > f_k$ . Equation (7) can be substituted into Eq. (5), leading to the next equation:

$$\tan \phi = f_s, \quad (8)$$

which relates that the friction of a group of particles is limited by the internal angle whose tangent is the same as the coefficient of static friction.

The second term of Eq. (5) describes the cohesion  $C$  between the particle surfaces, which is the capacity of a surface to stick together with other material surfaces by

capillary (attraction forces between liquids and surfaces). In this study, our focus is on noncohesive materials with small values of  $C$ , and with particular emphasis on materials with a high internal friction angle. Ground coffee is capable of reaching up to  $45^\circ$  of internal friction angle [18].

### C. Mohr-Coulomb failure criterion

The Mohr-Coulomb failure envelope is limited by normal stresses, which can be decomposed into circles whose diameters are formed by the maximum principal  $\sigma_1$  stress and minimum principal stress  $\sigma_3$  [69]. The diameters determine the effective stress required to maintain the mass in equilibrium. As long as the shear stress remains below the failure envelope the mass material will stay in equilibrium. Mohr-Coulomb circles are experimentally obtained in triaxial compression, and extension tests [70,71]. The triaxial tests can be subjected to various confining pressures representing the minor principal stress  $\sigma_3$  in triaxial compression tests, and the major principal stress  $\sigma_1$  in triaxial extension tests. Figure 10 shows a region of granular material aligned to the principal planes and axes. The relationship between the principal stress axes and the shear stress planes is as follows:

$$\sigma_n = \frac{\sigma_1 + \sigma_3}{2} + \frac{\sigma_1 - \sigma_3}{2} \cos 2\alpha, \quad (9)$$

$$\tau_s = \frac{\sigma_1 - \sigma_3}{2} \sin 2\alpha. \quad (10)$$

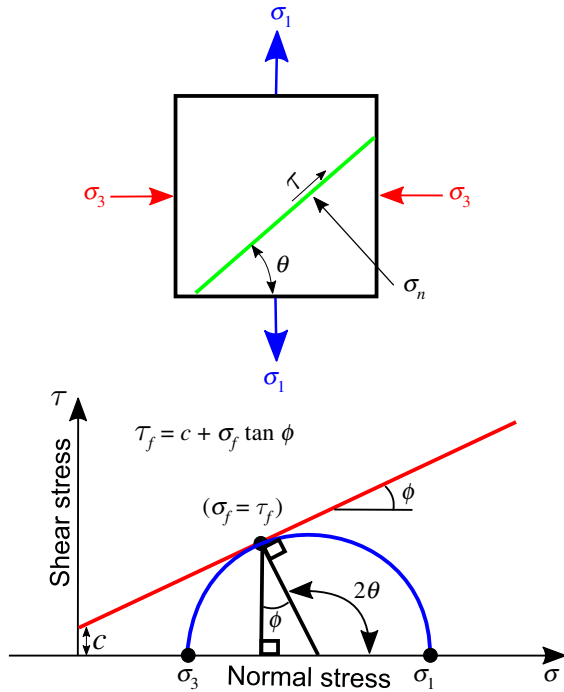


FIG. 10. Mohr-Coulomb circles.

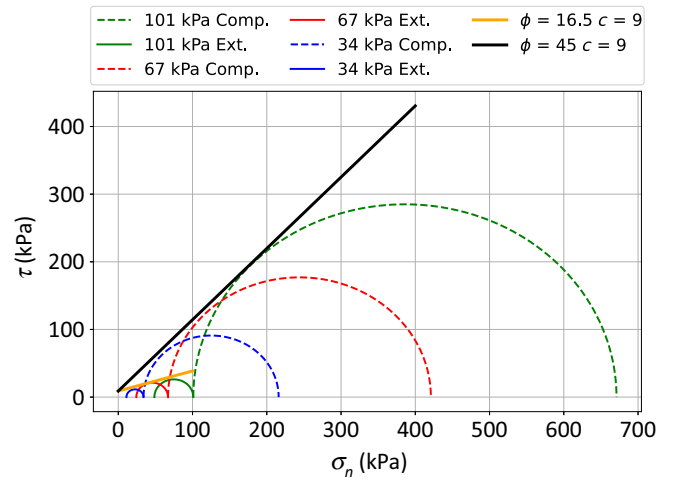


FIG. 11. Triaxial compression and extension tests.

Figure 11 shows the Mohr-Coulomb circles for various levels of confining pressure in triaxial compression and extension tests for ground coffee (the underlying data for these generated plots is taken from Cheng [18]). The red line from Fig. 11 represents the Mohr-Coulomb failure envelope in triaxial compression, and the yellow line represents the failure envelope in triaxial extension. The direction of the failure is analyzed by using principal stress trajectories.

### D. Stress analysis

In order to apply the failure criteria to the VPP beams, we must first transform the stresses calculated by the beam model into principal stresses. Figure 12(a) shows the shear force and bending moment diagrams for the four-point bending beams studied here. A specific element of the beam can be subjected to different normal- and shear-stress distributions. The maximum normal stress and the minimum shear stress are found on the top (tension) and bottom (compression) beam layers. Whereas the maximum shear stress is found in the neutral axis. Any combination of shear and normal stresses can be transformed into principal stresses by using Mohr's circles, and the trajectories of the principal stresses can be drawn by following the tangent of every single point element in principal directions [see Fig. 12(b)].

Figure 12(c) shows the trajectories of the principal stresses for a prismatic beam; the beam stress-state transformation creates two principal stress trajectories passing through each point. The trajectories are perpendicular from each other since the principal stresses are defined orthogonally. One of the curves represents the tensional trajectories, and the other portrays compressive trajectories. Both trajectories may shift the principal major stress to the minor principal stress and vice versa when the stress trajectories pass through the neutral axis. In other words,

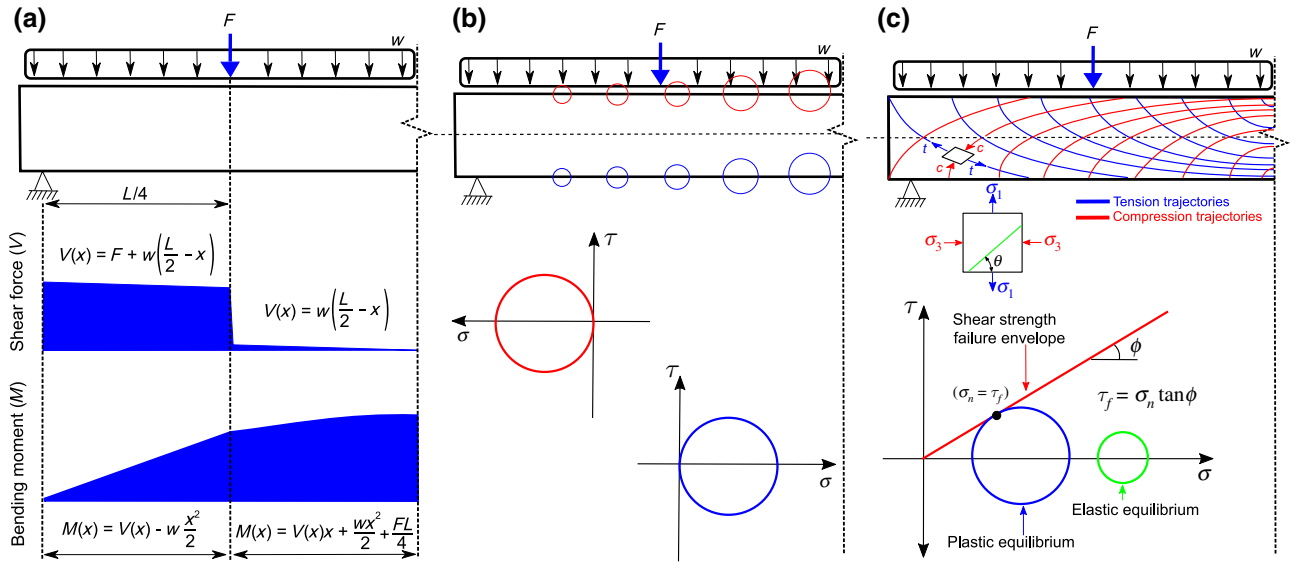


FIG. 12. (a) First step: stresses on  $xy$  coordinates. (b) Second step: transformation of normal stresses to principal stresses. (c) Third step: principal stresses trajectories and failure analysis.

tensile trajectories will be major principal stresses below the neutral axis and will be minor principal stresses above the neutral axis. On the other hand, for vacuum-packed particle beams, the confining pressure due to vacuum represents the major principal stress on the lowest part of the beam, and it represents the minor principal stress on the uppermost part of the beam.

The failure for any section of the beam can be known from the deviatoric stress ( $q$ ), which represents the diameter of the Mohr circles and follows the same definition from Eq. (2b):

$$q = \sigma_1 - \sigma_3. \quad (11)$$

The failure occurs when the following condition is reached:

$$q \geq q^*. \quad (12)$$

The yielding stress  $q^*$  occurs when  $\tau = \tau_{\max}$  and  $2\alpha = (\pi/2) + \phi$ . In triaxial compression, the maximum normal stress ( $\sigma_{\max}$ ) that the grains can sustain under a confining pressure ( $\sigma_3$ ) can be calculated from the following equation:

$$\sigma_{\max} = \sigma_3 \tan^2 \left( \frac{\pi}{4} + \frac{\phi}{2} \right) + 2C \tan \left( \frac{\pi}{4} + \frac{\phi}{2} \right). \quad (13)$$

For the triaxial extension, the vacuum pressure becomes the major principal stress ( $\sigma_1$ ).

$$\sigma_{\max} = \sigma_1 \tan^2 \left( \frac{\pi}{4} - \frac{\phi}{2} \right) - 2C \tan \left( \frac{\pi}{4} - \frac{\phi}{2} \right). \quad (14)$$

Figure 13(a) shows a vacuum-packed beam subjected to a bending moment around the  $z$  axis. Three distinct stress conditions are shown as the bending moment increases from the end to the middle section of the beam. The first condition is found on plane  $A$  in Fig. 13(b). As the load increases, the compressive stress on the top increases and the stress on the bottom decreases. For this condition, the curvature of the beam is given by the following equation:

$$\kappa = \frac{\varepsilon_t - \varepsilon_b}{h} = \frac{\sigma_t - \sigma_b}{Eh}, \quad (15)$$

where  $\sigma_t$  is the stress on top, and  $\sigma_b$ , is the stress on the bottom of the beam. Both stresses can be easily calculated by equilibrium forces and transform in total stress coordinates by adding up the effective stress.

$$\sigma_t = P_V - \sigma_n + \frac{M}{Z}, \quad (16)$$

$$\sigma_b = P_V - \sigma_n - \frac{M}{Z}, \quad (17)$$

where  $Z$  is the section modulus. The vacuum pressure  $P_V$  resembles the hydrostatic part of the stress vector from Eq. (1a). The deviatoric stress from Eq. (2a) can be formed by subtracting the hydrostatic term  $S_{xy} = P_V - \sigma_n$  to simplify Eqs. (16) and (17) into the next equations:

$$\sigma_t = S_{xy} + \frac{M}{Z} \quad (18)$$

$$\sigma_b = S_{xy} - \frac{M}{Z}. \quad (19)$$

The deviatoric stress in  $xy$  coordinates resembles the yielding stress for the triaxial extension test when it is

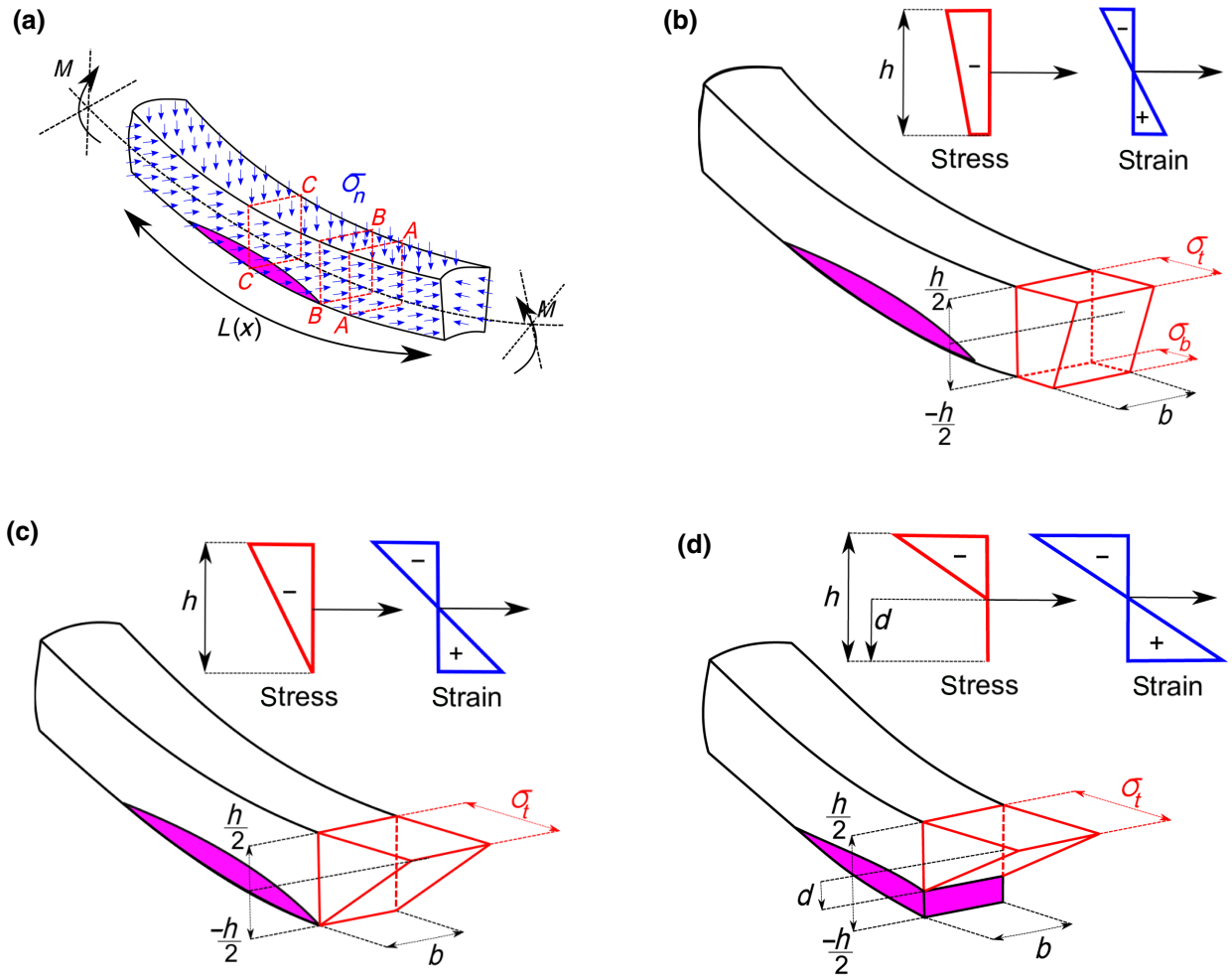


FIG. 13. (a) Vacuum-packed particle beam on bending, (b) first stress-strain condition, (c) second stress-strain condition, (d) third stress-strain condition.

transformed into principal stresses.

$$S_{xy} \implies q. \quad (20)$$

When the bending moment increases the compressive stress on the bottom decreases until zero [plane B from Fig. 13(c)].

$$\sigma_b = S_{xy} - \frac{M}{Z} = 0. \quad (21)$$

The rupturing moment of the beam can be known by isolating  $M$  from Eq. (21).

$$M_s = ZS_{xy}. \quad (22)$$

If the bending moment increases to the point where it overcomes the splitting moment  $M_s$ , the grains will split away ( $q > q^*$ ), reducing the cross-section area. In this analysis, once splitting has started, the second moment of area will

vary along the span and as load increases due to the reduction in load-bearing material. The reduction is determined by the distance  $d$ . The stress over a distance of  $d$  is shown on plane C in Fig. 13(d) and is given by the following equation:

$$\sigma = \frac{\sigma_t}{(h/2) - d}y - \frac{\sigma_t}{(h/2) - d}d. \quad (23)$$

The stress on top of the beam  $\sigma_t$  and the distance  $d$  are calculated by equilibrium forces and the sum of the moments around the point of zero stress.

$$S_{xy}wh = \int_d^{h/2} (\sigma h)dy = -\frac{(2d - h)w\sigma_t}{4}, \quad (24)$$

$$M = \int_d^{h/2} (\sigma hy)dy = -\frac{w\sigma_t(d + h)[d - (h/2)]}{6}. \quad (25)$$

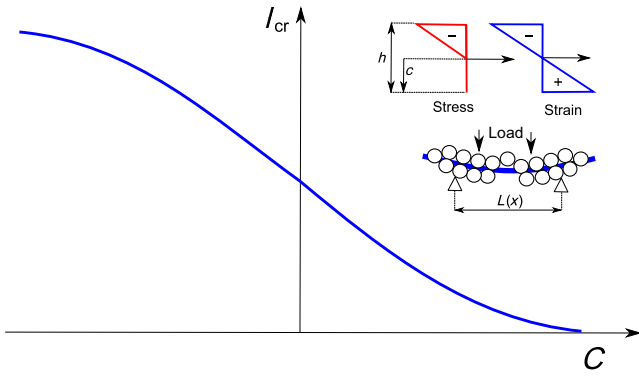


FIG. 14. Decreasing of the second moment of area.

Isolating  $\sigma_t$  and equaling both terms from Eqs. (24) and (25) leads to the solution of distance  $d$ .

$$\sigma_t = -\frac{4S_{xy}^2 h^2 w}{3(2M - S_{xy} w h^2)} \quad (26)$$

$$d = \frac{3M}{whS_{xy}} - h. \quad (27)$$

The decrease of the second moment of area for the condition on plane  $C$  can be expressed in terms of the distance  $d$ :

$$I_{cr} = \frac{w[(d+h)(2d-h)^2]}{24}. \quad (28)$$

Equation (28) is plotted in Fig. 14 and is indeterminate when the bending moment reaches the next condition:

$$M = \frac{S_{xy} w h^2}{2}. \quad (29)$$

### E. Model results

To model the flexural tests from Sec. III, the VPPB model is implemented numerically using the trapezoid rule to integrate the Euler-Bernoulli beam theory equations. The failure mechanism is implemented into the model using Eqs. (13), (14), and (28) to calculate the yielding stresses and curvature at any vacuum pressure level. The internal friction angle and the cohesion parameters are taken from the triaxial compression tests performed by Cheng [18] (see Fig. 11). Table IV shows all the material inputs required for the analysis. The model is compared

TABLE IV. VPPB model inputs.

$\phi$	$C$	$q^*(23 \text{ kPa})$	$q^*(52 \text{ kPa})$	$q^*(75 \text{ kPa})$	$q^*(91 \text{ kPa})$
16.5°	9.0	19 kPa	40 kPa	58 kPa	63 kPa

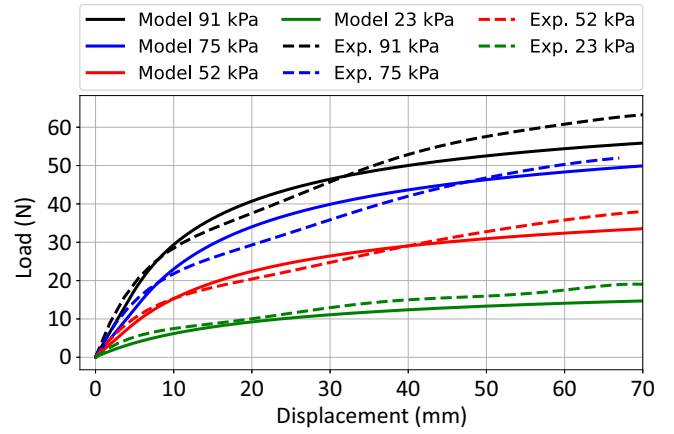


FIG. 15. VPPB model and experimental comparison results.

with the beam samples at various vacuum pressure levels (23–91 kPa). Figure 15 displays the comparison results between the experimental data and the VPPB model. In general, it can be seen that the complex softening behavior is fairly well captured over the range of pressures tested, although there are some differences in shape as the displacement evolves. Overall, this model has an average error of less than 8%, found using Eq. (30).

$$E_r = \frac{\sigma_{\text{model}} - \sigma_{\text{test}}}{\sigma_{\text{test}}}. \quad (30)$$

The repeatability of the model is determined by the packing fraction and cohesion parameters, which are used as material inputs in the model. These input parameters can be used to analyze a wide variety of materials by considering the deviatoric stresses at various vacuum levels; thus, the failure mechanism due to zero-stress state condition may capture the nonlinear softening region for a large number of vacuum-packed particle-beam applications. On the other hand, the performance of the VPPB model can be tweaked by altering the mechanical inputs. In this case, the relative error between the experimental data and the VPPB model can be reduced by tweaking the packing fraction and cohesion parameters within a small margin; however, we leave those parameters fixed directly from the experimental results to provide a common reference and a means of comparing the relative error for the next plasticity model, which calculates its material inputs using the same experimental data.

## IV. THE CONTINUUM APPROACH—FINITE-ELEMENT ANALYSIS USING THE JC- $p$ MODEL

The following section describes another model to analyze the flexural stiffness of VPP structures using a continuum mechanics approach based on plasticity. Based on our VPP behavior observations in Ref. [1], we can consider

VPP behavior as an elastoplastic material with strain rate hardening and temperature softening. Additionally, from previous research [72], the material showed an isotropic coupling from tensile and compression properties, which forces an asymmetric position of the neutral axis in order to maintain force balance. Based on the previous statements, the plasticity model is explained by a set of equations related to its deformation.

$$\phi = \frac{1}{2} s_{ij} s_{ij} - \frac{\sigma_{y+/-}(\epsilon, \dot{\epsilon}, T, p)^2}{3} \leq 0, \quad (31)$$

$$\sigma_{y+/-}(\epsilon, \dot{\epsilon}, T, p) = \begin{cases} \sigma_{y+}(\epsilon, \dot{\epsilon}, T, p) & \text{if } I_\sigma > 0 \\ \sigma_{y-}(\epsilon, \dot{\epsilon}, T, p) & \text{if } I_\sigma < 0, \end{cases} \quad (32)$$

where  $\phi$  is the plasticity function,  $s_{ij}$  is the deviatoric components of stress tensor,  $\sigma_{y+/-}(\epsilon, \dot{\epsilon}, T, p)$  is the radius of plasticity function,  $\epsilon$  is strain,  $\dot{\epsilon}$  is strain rate,  $T$  is temperature,  $p$  is underpressure, and  $I_\sigma$  is the first invariant of stress tensor.

Equation (31) is an extension of the von Mises yield criterion where the plasticity surface is in cylindrical shape with a variable radius (illustrated in Fig. 16) that depends on material parameters (strain, strain rate, temperature, and vacuum pressure).

Additionally, by extending Eq. (31) with Eq. (32) it is possible to include the effects of the asymmetric location of the neutral axis by using a stress sign (tension and compression) component on the material behavior. The relation  $\sigma_{y+/-}(\epsilon, \dot{\epsilon}, T, p)$  is developed to describe the nonlinear physics of the VPP structure and is given by Eq. (33), which is a modification of the original Johnson-Cook model [73]. The modified model is constructed to include strain rate, temperature, and vacuum pressure parameters. These parameters are used to determine the radius of the

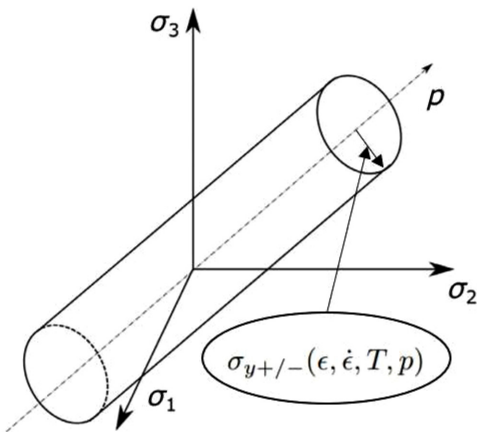


FIG. 16. Illustration of plasticity surface for VPP.

plasticity surface:

$$\sigma(\epsilon, \dot{\epsilon}, T, p) = [\alpha + \beta p + (\Psi + \gamma p)\epsilon^{\Upsilon - \chi p}] \left[ 1 + (\Xi - \mu p) \ln\left(\frac{\dot{\epsilon}}{\dot{\epsilon}_0}\right) \right] \left[ 1 - \left(\frac{T - T_R}{T_m - T_R}\right)^{\eta p^\psi} \right], \quad (33)$$

where  $\alpha, \beta, \Psi, \gamma, \Upsilon, \chi, \Xi, \mu, \eta, \psi$  are material constants.

The previously mentioned equations are implemented into the commercial finite-element code LS-DYNA by modifying the material model library mat\_124. To perform the flexural analysis, it is appropriate to initially define the model parameters on the basis of the triaxial compression and extension tests. The strain rate and temperature influence are not considered in this work; therefore, only six of the listed parameters have to be identified. Since the beam content is coffee grinds, the data provided in Ref. [18] is used to perform the identification procedure. The identification procedure is based on a nonlinear least-squares minimization and curve-fitting algorithm written in the python programming language.

The identification process starts with the parameters  $\alpha$  and  $\beta$ . It is carried out by obtaining the optimum parameters that can better match the yield stress solution at 0.2% of strain. These conditions are calculated separately for vacuum pressures from 34 to 101 kPa. The corresponding parameters  $\Psi, \gamma, \Upsilon, \chi$  are found using the same previous procedure. However, the multiobjective function that minimizes the solution consists of two parameter pairs defined by the sum  $\Psi + \gamma p$  and  $\Upsilon - \chi p$ . Then, the procedure is repeated analogously for tension stress state.

All identified parameters are listed in Table V. Additionally, Fig. 17 shows the comparison results of the model and test results under selected vacuum pressure levels of 34 and 67 kPa for triaxial compression, and 34 kPa for the triaxial extension.

According to the comparative results, the relative error [calculated from Eq. (30)] for any vacuum pressure condition is less than 10% along the full stress-strain envelope. These comparative results suggest that the material parameters for coffee grains are correctly defined and introduced as material parameters for the flexural FEA.

The FEA model is shown in Fig. 18. The beam is meshed with fully integrated hexagonal elements with an average size of 3 mm. The applied boundary conditions and loading conditions are analogous to the experimental tests from Sec. II. The supports are constrained in the vertical and transverse directions to avoid rigid body motion.

TABLE V. Material constants.

$\alpha_-$	$\beta_-$	$\Psi_-$	$\gamma_-$	$\Upsilon_-$	$\chi_-$
0.000 085	0.204	0.16	16.4	0.8	0.76
$\alpha_+$	$\beta_+$	$\Psi_+$	$\gamma_+$	$\Upsilon_+$	$\chi_+$
0.0027	0.024	0.03	0.84	0.87	4.69

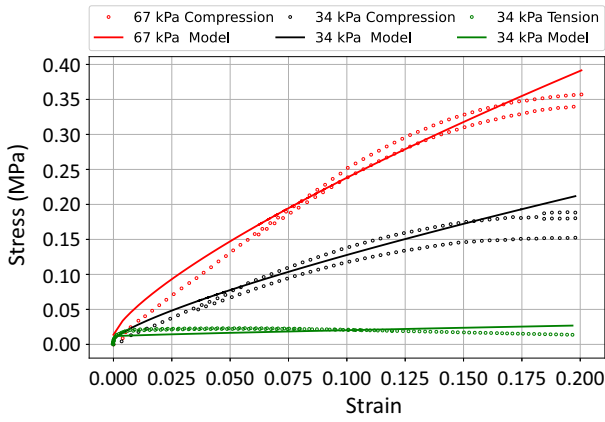


FIG. 17. Model [Eq. (33)] after parameter identification and test [18] results' comparison.

The gripper rollers device with a kinematic loading of 16 mm/s is used to simulate the testing machine's contact rollers. The simulations are performed on a PC with six cores of 2.4 GHz and 64 GB of ram. For each vacuum pressure test condition, the simulation takes approximately 2 h to finish.

Numerical tests are performed for the four vacuum pressure levels (23, 52, 73, and 91 kPa). Only the parameter  $p$  is changed during the simulations, with beam geometry, boundary conditions, and material properties held constant (Table V). Figure 18 shows the comparison of simulation and experimental results for different vacuum levels. The absolute error is calculated according to Eq. (30). The error is higher for lower vacuum pressure levels and reduces as the vacuum pressure increases. The maximum error for the 23 kPa condition is about 20%. For the higher vacuum pressure level, the maximum error is lower than 10%. Taking into account the simplicity of the material model and the complexity of nonlinear behavior, the model shows a satisfactory result.

The key benefit of the FEM simulation is that it can report three-dimensional stresses and strains, as shown in Figs. 20 and 21. Examining particular elements may reveal interesting features; for example, Fig. 21 displays stress concentrations on the top edge of the beam due to contact loading. The same figure also shows that tensile stresses

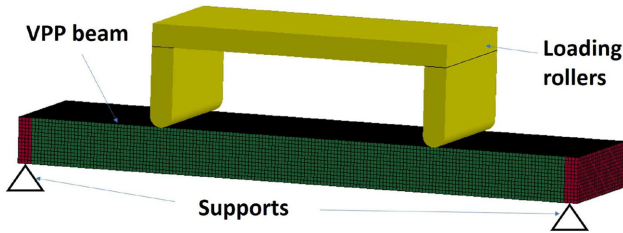


FIG. 18. FE model and boundary conditions.

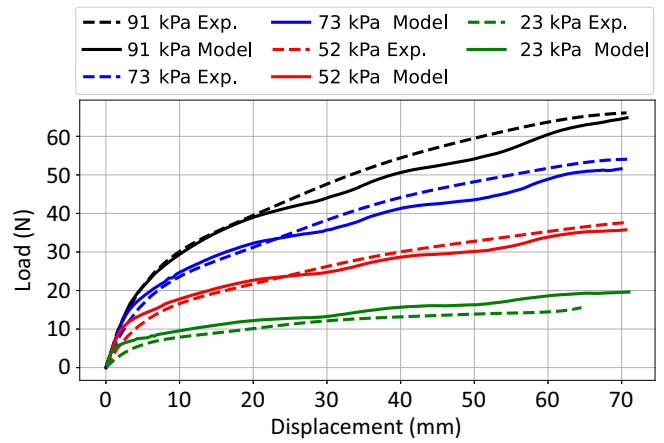


FIG. 19. Simulation and experiment comparison.

are significantly lower than the compressive stresses, which agrees with VPP model assumptions. Additionally, Fig. 21 shows the changes in strain distribution as the bending load increases. Moreover, Fig. 22 illustrates the strain and stress distribution across the height at the middle section of the beam. The stress-strain distribution is asymmetric despite the fact that the cross-section area is symmetrical, which implies a significant change of stiffness above and below the neutral axis. Nonetheless, the variation of the vacuum pressure can initially change the neutral axis position as the bending moment increases. Once again, it is confirmed that the presence of the compressive stress distribution is significantly higher in magnitude than the tensile stress distribution. These results are in line with the load-bearing capabilities of the grains to better withstand compression than tension forces, as seen in the experiments.

## V. DISCUSSION

### A. Assumptions and deficiencies of the VPPB model

The VPP beam model is a continuum model, which implies that the beam's mechanical properties are considered to remain constant throughout its length and that the

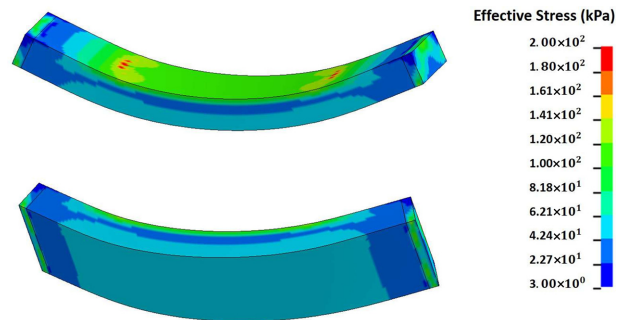


FIG. 20. Stress distribution for vacuum level of 91 kPa.

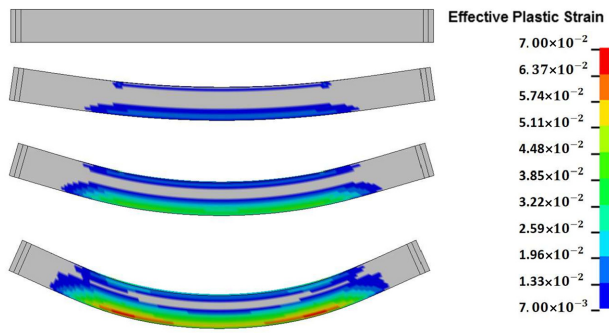


FIG. 21. Strain distribution.

overall stiffness is assumed to be proportional to the hydrostatic stress, in this case, the vacuum pressure. Another assumption is that the softening behavior is caused by the inability of the structure to resist the increase of the deviatoric stress, which is limited by the Mohr-Coulomb envelope and follows the assumptions of the critical state theory, according to which under constant stress the granular assembly keeps deforming in shear at constant volume. These assumptions allow the softening behavior to be easily captured by simply decreasing the second moment of area during loading and enabling the computation of a more efficient and straightforward model, capable of capturing the change in stiffness for a large number of smart structures.

One of the VPPM model’s shortcomings is that it implicitly substitutes the effects of dilatancy by considering the zero-stress condition throughout the principal stress trajectories, which leads to the decrease of the second moment of area; thus, although the softening behavior

is captured, the internal volume of the granular assembly (packing fraction) remains constant during consolidation and deformation under loading.

As previously stated, the Mohr-Coulomb analysis used in this research is based on critical state theory, which is not a constitutive model but rather a theoretical constitutive set of rules within which the zero-stress condition is developed; notwithstanding, additional constitutive relations and models can be added. The incorporation of spatially heterogeneous material properties and dilatation into the model may help to improve the results even further and account for volume change. In particular, when the volume fraction varies over the width of the beam under load and consolidation due to vacuum pressure, the mechanical characteristics of the beam will change as a result.

Dilatancy state lines can be used to capture the volume variations in the VPPB model by including a fabric tensor and a state parameter that quantifies the distance between critical state values in terms of void ratios and pressure. The inclusion of these dilatancy state lines into the model can take into consideration the anisotropic properties of the granular assembly at the critical state, which improves the critical value criterion used in classical state theory. For example, the anisotropic critical state model developed by Xiang *et al.* [38] can be used for this regard. The implementation of the dilatancy state lines into the VPPB model can be done during the principal stress trajectories analysis, which can be used to predict not only failure at critical state due to a significant increase in deviatoric stress, but also the variation of packing fraction as the hydrostatic pressure changes as well.

**B. Comparison between VPPB and JC-*p* models**

Having presented two different approaches to modeling the complex nonlinear response of VPP beam structures under flexural loads, those being the proposed analytical VPPB model and the Johnson Cook with pressure parameter (JC-*p*) material model applied to FEA, it is useful here to discuss their relative merits.

Both models depend on experimentally measured material properties taken from triaxial compression tests, but to different extents. The JC-*p* method uses the yield stress to determine the material constants needed to describe the plasticity surface’s radius. In contrast, the VPPB method employs the yield stress as a failure condition using trajectories of the principal stresses, and then uses shear failure to predict the progressive reduction in the second moment of area as an increasingly large region of the material becomes ineffective at carrying load.

Both methods suggest that compression is the dominant load-carrying mode for VPP structures, which is realized as shear forces between individual grains. This is in line with the triaxial tension and compression test results

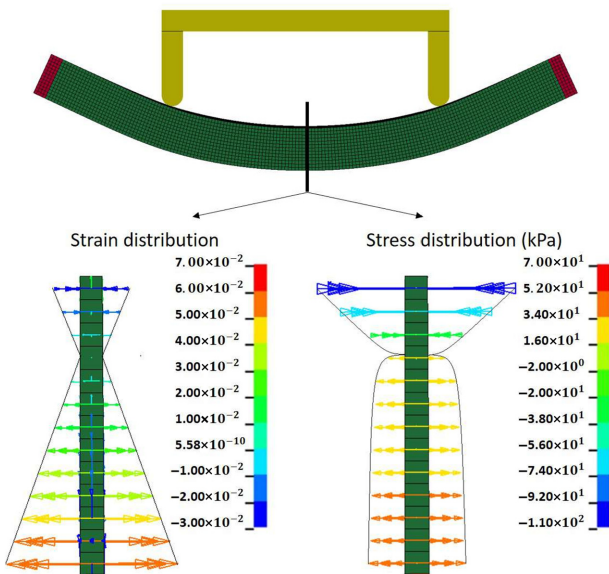


FIG. 22. Strain and stress distribution for a vacuum level of 91 kPa.

[1,18]. Figure 22 from the JC- $p$  model shows only a very small change in the tensile stress as the bending moment increases, while the compressive stress increases significantly. This aspect of the JC- $p$  results align with the stress distribution shown in Fig. 13 from the VPPB model, which made key assumptions around compressive stress loading.

Another essential aspect both models can predict is the neutral axis shifting under loading and as a function of applied vacuum pressure. The VPPB model explained that the neutral axis shifts upwards as the bending moment increases due to grain motion. On the other hand, the JC- $p$  model explains that the first stress invariant shifts the neutral axis. Since there are no applied external forces in the longitudinal direction of the beam, the sum of stress forces in that direction must also be zero. To maintain this balance, assuming that the material properties for compression and tension are different, the neutral axis must shift.

Figure 23 displays the absolute error [Eq. (30)] in both models for a vacuum pressure of 91 kPa. The dashed lines are the average error values. Table VI indicates the maximum and average errors of both models at all of the vacuum pressure levels considered. The numbers confirm that the average error for the JC- $p$  model decreases as vacuum pressure increases, while the average errors remain slightly constant for the VPPB model. However, for the pressure level of 23 kPa, the error has increased considerably in both models.

One further advantage of the JC- $p$  model is that it can also identify stress and strain distribution in all three directions, which may be particularly useful for more complex VPP structures. In comparison, the VPPB model is essentially two dimensional, and so can only evaluate in-plane strain and stress. However, the simpler, parametrically defined, and analytical nature of the VPPB model means that it is faster to implement, and can more easily handle changes in geometry or material properties. It

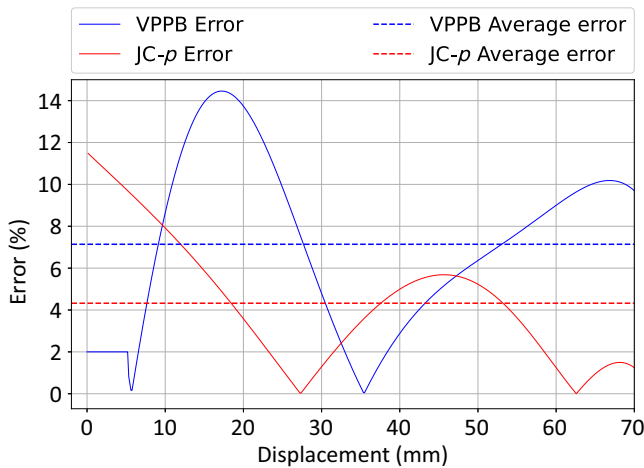


FIG. 23. Error along the deformation for a confining pressure of 91 kPa.

TABLE VI. Average error and maximum error for each vacuum pressure.

Model	Vacuum (kPa)	Average error (%)	Maximum error (%)
VPPB	23	16.8	23
VPPB	52	7.4	12
VPPB	75	7.2	17.5
VPPB	91	7.1	14.2
JC- $p$	23	9	20
JC- $p$	52	7	17.5
JC- $p$	75	4.8	15
JC- $p$	91	4.3	11.5

is therefore particularly useful for early design exploration and optimization after which the JC- $p$  FEA can be used to explore the response of a more focused range of parameters in more detail. In terms of computational cost, the VPPB model can solve for the displacement curve of particular combination of material, geometry, and pressure loading in a matter of seconds (on a single core 2 GHz CPU with 8 GB of RAM), while the FEA JC- $p$  model requires approximately 2 h for each condition (on a six-core 2.4-GHz CPU and 64 GB of ram).

Clearly, both models are useful for estimating the highly nonlinear behavior of vacuum-packed particle beams, and both are successfully able to capture the progressively developing softening behavior induced by shear failure and motion between particles, with the fundamental trade-off being between speed and accuracy and detail—as is often the case. They should both prove useful in future work on the development of bending-dominated smart structures employing granular jamming to provide variable stiffness.

## VI. CONCLUSIONS

This work seeks to expand our understanding of the mechanics of vacuum-packed particles under flexural loading, so that the concept of granular jamming can be more widely applied to smart structures as a means of creating variable stiffness. In order to do this, the most detailed experiments to date on flexural properties of VPP beams are undertaken, and in parallel two different modeling methods are employed to predict the mechanical response of the same VPP beam. Full-field strain data from a digital-image-correlation system reveal a complex evolution of strains across the beam with dependencies on pressure and loading. While a roughly linear distribution of stress is seen in the axial direction, the transverse direction reveals a nonlinear strain distribution, which provides evidence of particle motion above a pressure-dependent critical load condition. This particle motion shows up as a thinning of the cross-section area and movement of the neutral axis. This then leads to reduced stiffness and a plateauing in

load-carrying capability. These findings inspired the creation of an analytical model (VPPB model) that allows the softening nonlinear to be captured by reducing the second moment of inertia and also motivated the study and comparison using a nonlinear FEA based on the JC- $p$  model of material plasticity. The experimental results and the comparison between modeling methods reveal the following key conclusions:

(a) The variation in stiffness of the VPP beams can be increased by more than 4 times from a vacuum pressure of 20 to 91 kPa.

(b) Changing skin thickness, over the range tested and for this geometry and loading condition, did not have an appreciable effect on the mechanical response of the VPP beam.

(c) Grain motion is calculated indirectly from the skin using DIC. Full-field strain maps reveal a slippage of the grains emerging at the bottom of the beam (where tensile stresses would typically be expected) and increasing in a nonlinear manner as the bending load increases.

(d) An analytical model of VPP beams combining methods from beam theory, inflatable structures, and soil mechanics is developed and implemented.

(e) The proposed models are effective in capturing nonlinear stiffness at different vacuum levels. The simulation results for both models show useful levels of accuracy, with an average error of less than 10% for both, but with generally better accuracy from the higher fidelity JC- $p$  FEA.

(f) The stress distribution of the VPPB and JC- $p$  models is primarily based on compressive stress, and the maximum is contained in the uppermost part of the beam. For both models, tensile stress is relatively low in comparison to compressive stress, since the grain cannot hold a large amount of tensile stress. This conclusion is consistent with the experimental results.

(g) Both models can capture the experimentally observed movement of the neutral axis moves upwards under increasing load as the portion of the beam that is under tension (and therefore not effectively carrying load) increases.

(h) The JC- $p$  model can show the stress and strain distribution in all directions. The VPPB model, on the other hand, is a much simpler model that can only display an in-plane stress distribution but is easier to implement and computationally faster.

In conclusion, using granular jamming of vacuum-packed particles as a variable stiffness mechanism can open up a whole different variety of conceivable options for smart and adaptive structures. Before being a viable solution however, we must first be able to predict the complex and highly nonlinear response of these systems, especially when large deformations are required. It is hoped that

the models proposed here will serve as useful tools in that regard, as they provide a good level of accuracy for a modest amount of complexity, with the VPPB model providing marginally less accuracy but with a simpler, analytical formulation. In future work it would be worthwhile to develop the proposed FEA constitutive model of the granular-jamming mechanism. The continuum model should include the granular breaking parameter, which causes the structure softening [74]. It could be done by modification of Eq. (32) and taking into account the influence of the first invariant on the value of the radius of the plasticity surface or replacing it, for example, with the Burzynski-Drucker-Prager model described in Ref. [75]. This model is additionally able to include the dilatancy, which is an undoubted advantage over the approach presented in this work.

Nevertheless, this work is currently ongoing to apply these models to more complex structural designs for morphing aircraft control surfaces in order to show the ability of variable stiffness to provide a feasible compromise between low-energy requirements for actuation and high resistance to deformation under external loading.

- 
- [1] R. Zalewski, Constitutive model for special granular structures, *Int. J. Nonlinear Mech.* **45**, 279 (2010).
  - [2] S.-Q. An, H.-L. Zou, Z.-C. Deng, and D.-Y. Guo, Damping effect of particle-jamming structure for soft actuators with 3D-printed particles, *Smart Mater. Struct.* **29**, 095012 (2020).
  - [3] L. Li, Z. Liu, M. Zhou, X. Li, Y. Meng, and Y. Tian, Flexible adhesion control by modulating backing stiffness based on jamming of granular materials, *Smart Mater. Struct.* **28**, 115023 (2019).
  - [4] I. Svetel, Prof. Ivan Petrovic, PhD, M. Arch (1932–2000), *Autom. Constr.* **2**, 129 (2002).
  - [5] N. G. Cheng, M. B. Lobovsky, S. J. Keating, A. M. Setapen, K. I. Gero, A. E. Hosoi, and K. D. Iagnemma, in *2012 IEEE International Conference on Robotics and Automation* (IEEE, Saint Paul, MN, USA, 2012), p. 4328.
  - [6] E. Brown, N. Rodenberg, J. Amend, A. Mozeika, E. Steltz, M. R. Zakin, H. Lipson, and H. M. Jaeger, Universal robotic gripper based on the jamming of granular material, *Proc. Natl. Acad. Sci. U.S.A.* **107**, 18809 (2010).
  - [7] A. J. Loeve, O. S. van de Ven, J. G. Vogel, P. Breedveld, and J. Dankelman, Vacuum packed particles as flexible endoscope guides with controllable rigidity, *Granul. Matter* **12**, 543 (2010).
  - [8] L. Blanc, A. Pol, B. François, A. Delchambre, P. Lambert, and F. Gabrieli, in *Micro to MACRO Mathematical Modelling in Soil Mechanics* (Springer, Gewerbstrasse 11, 6330 Cham, Switzerland, 2018), p. 57.
  - [9] J. D. Brigido-González, S. G. Burrow, and B. K. Woods, Switchable stiffness morphing aerostructures based on granular jamming, *J. Intell. Mater. Syst. Struct.* **30**, 2581 (2019).
  - [10] B. K. S. Woods and M. I. Friswell, in *Smart Materials, Adaptive Structures and Intelligent Systems*, Vol. 45103

- (American Society of Mechanical Engineers, Stone Mountain, Georgia, USA, 2012), p. 555.
- [11] A. E. Rivero, S. Fournier, M. Manolesos, J. E. Cooper, and B. Woods, in *AIAA Scitech 2020 Forum* (American Institute of Aeronautics and Astronautics, Florida, USA, 2020), p. 1300.
- [12] P. Bartkowski and R. Zalewski, in *MATEC Web of Conferences*, Vol. 254 (EDP Sciences, Rydzyna, Poland, 2019), p. 05008.
- [13] F. Huijben, F. Van Herwijnen, and R. Nijse, in *Proceedings of International Conference on Textile Composites and Inflatable Structures, Stuttgart*, E. Oñate, and B. Kröplin, (Eds) (CIMNE, Stuttgart, 2009).
- [14] S. M. Z. Sayyadan, F. Gharib, and A. Garakan, in *2017 22nd International Conference on Methods and Models in Automation and Robotics (MMAR)* (IEEE, Miedzyzdroje, Poland, 2017), p. 396.
- [15] A. Jiang, T. Ranzani, G. Gerboni, L. Lekstutyte, K. Althofer, P. Dasgupta, and T. Nanayakkara, *Robotic granular jamming: Does the membrane matter?*, *Soft Robot.* **1**, 192 (2014).
- [16] F. Huijben, PhD thesis, Eindhoven University of Technology, 2014.
- [17] P. Bartkowski, R. Zalewski, and P. Chodkiewicz, Parameter identification of Bouc-Wen model for vacuum packed particles based on genetic algorithm, *Arch. Civ. Mech. Eng.* **19**, 322 (2019).
- [18] N. G. Cheng, PhD thesis, Massachusetts Institute of Technology, 2013.
- [19] A. G. Athanassiadis, M. Z. Miskin, P. Kaplan, N. Rodenberg, S. H. Lee, J. Merritt, E. Brown, J. Amend, H. Lipson, and H. M. Jaeger, Particle shape effects on the stress response of granular packings, *Soft Matter* **10**, 48 (2014).
- [20] J.-F. Camenen and Y. Descantes, Geometrical properties of rigid frictionless granular packings as a function of particle size and shape, *Phys. Rev. E* **96**, 012904 (2017).
- [21] L. Lopatina, C. O. Reichhardt, and C. Reichhardt, Jamming in granular polymers, *Phys. Rev. E* **84**, 011303 (2011).
- [22] L. Zhang, Y. Wang, and J. Zhang, Force-chain distributions in granular systems, *Phys. Rev. E* **89**, 012203 (2014).
- [23] M. Cates, J. Wittmer, J.-P. Bouchaud, and P. Claudin, Jamming, Force Chains, and Fragile Matter, *Phys. Rev. Lett.* **81**, 1841 (1998).
- [24] J. Peters, M. Muthuswamy, J. Wibowo, and A. Tordesillas, Characterization of force chains in granular material, *Phys. Rev. E* **72**, 041307 (2005).
- [25] S. Atkinson, F. H. Stillinger, and S. Torquato, Detailed characterization of rattlers in exactly isostatic, strictly jammed sphere packings, *Phys. Rev. E* **88**, 062208 (2013).
- [26] S. Torquato, T. M. Truskett, and P. G. Debenedetti, Is Random Close Packing of Spheres Well Defined?, *Phys. Rev. Lett.* **84**, 2064 (2000).
- [27] J. Desrues, A. Argilaga, D. Caillerie, G. Combe, T. K. Nguyen, V. Richefeu, and S. Dal Pont, From discrete to continuum modelling of boundary value problems in geomechanics: An integrated FEM-DEM approach, *Int. J. Numer. Anal. Methods Geomech.* **43**, 919 (2019).
- [28] A. B. Vesic and W. H. Johnson, Model studies of beams resting on a silt subgrade, *J. Soil Mech. Found. Div.* **89**, 1 (1963).
- [29] M. E. Harr, J. L. Davidson, D.-M. Ho, L. E. Pombo, S. Ramaswamy, and J. C. Rosner, Euler beams on a two parameter foundation model, *J. Soil Mech. Found. Div.* **95**, 933 (1969).
- [30] A. Ajaz and R. Parry, Analysis of bending stresses in soil beams, *Geotechnique* **25**, 586 (1975).
- [31] P. Maheshwari, P. Basudhar, and S. Chandra, Analysis of beams on reinforced granular beds, *Geosynth. Int.* **11**, 470 (2004).
- [32] R. I. Borja, Analysis of incremental excavation based on critical state theory, *J. Geotech. Eng.* **116**, 964 (1990).
- [33] E. Magnucka-Blandzi, Critical state of a thin-walled beam under combined load, *Appl. Math. Model.* **33**, 3093 (2009).
- [34] D. M. Wood, *Soil Behaviour and Critical State Soil Mechanics* (Cambridge University Press, Trumpington street, Cambridge CB2 1RP, 1990).
- [35] D. Kolymbas, *Constitutive Modelling of Granular Materials* (Springer Science & Business Media, Berlin, Germany, 2012).
- [36] R. Wan and P. Guo, A simple constitutive model for granular soils: Modified stress-dilatancy approach, *Comput. Geotech.* **22**, 109 (1998).
- [37] R. F. Scott, Plasticity and constitutive relations in soil mechanics, *J. Geotech. Eng.* **111**, 559 (1985).
- [38] X. S. Li and Y. F. Dafalias, Anisotropic critical state theory: Role of fabric, *J. Eng. Mech.* **138**, 263 (2012).
- [39] W. Zhou, J. Liu, G. Ma, and X. Chang, Three-dimensional DEM investigation of critical state and dilatancy behaviors of granular materials, *Acta Geotech.* **12**, 527 (2017).
- [40] R. Wang, Y. F. Dafalias, P. Fu, and J.-M. Zhang, Fabric evolution and dilatancy within anisotropic critical state theory guided and validated by DEM, *Int. J. Solids Struct.* **188**, 210 (2020).
- [41] M. Madadi, O. Tsoungui, M. Lätzel, and S. Luding, On the fabric tensor of polydisperse granular materials in 2D, *Int. J. Solids Struct.* **41**, 2563 (2004).
- [42] Y. F. Dafalias, Must critical state theory be revisited to include fabric effects?, *Acta Geotech.* **11**, 479 (2016).
- [43] X. S. Li and Y. F. Dafalias, Dilatancy for cohesionless soils, *Géotechnique* **50**, 449 (2000).
- [44] K. Been and M. G. Jefferies, A state parameter for sands, *Géotechnique* **35**, 99 (1985).
- [45] D. M. Wood and K. Belkheir, Strain softening and state parameter for sand modelling, *Géotechnique* **44**, 335 (1994).
- [46] J. R. F. Arthur, J. I. Rodriguez del C, T. Dunstan, and K. S. Chua, Principal stress rotation: A missing parameter, *J. Geotech. Eng. Div.* **106**, 419 (1980).
- [47] M. Yoshimine, K. Ishihara, and W. Vargas, Effects of principal stress direction and intermediate principal stress on undrained shear behavior of sand, *Soils Found.* **38**, 179 (1998).
- [48] N. Mueggenburg, Granular compaction under confinement, *Phys. Rev. E* **85**, 041305 (2012).
- [49] S. Fazekas, J. Török, and J. Kertész, Critical packing in granular shear bands, *Phys. Rev. E* **75**, 011302 (2007).

- [50] D. Cantor, M. Cárdenas-Barrantes, I. Preechawuttipong, M. Renouf, and E. Azéma, Compaction Model for Highly Deformable Particle Assemblies, *Phys. Rev. Lett.* **124**, 208003 (2020).
- [51] S. Galindo-Torres, X. Zhang, and K. Krabbenhoft, Micromechanics of Liquefaction in Granular Materials, *Phys. Rev. Appl.* **10**, 064017 (2018).
- [52] C. W. MacMinn, E. R. Dufresne, and J. S. Wettlaufer, Large Deformations of a Soft Porous Material, *Phys. Rev. Appl.* **5**, 044020 (2016).
- [53] M. F. Nawaz, G. Bourrie, and F. Trolard, Soil compaction impact and modelling. A review, *Agron. Sustain. Dev.* **33**, 291 (2013).
- [54] H. Griffin and B. C. O’Kelly, Ground improvement by vacuum consolidation—A review, *Proc. Inst. Civ. Eng.—Ground Improv.* **167**, 274 (2014).
- [55] J. Chai, J. Carter, and S. Hayashi, Ground deformation induced by vacuum consolidation, *J. Geotech. Geoenviron. Eng.* **131**, 1552 (2005).
- [56] S. Silicones LTD, Superclear silicone sheet (2018). <https://www.silex.co.uk/products/>.
- [57] SMC, Pse53, sensor for multi channel controller (2019). <https://www.smc.eu/smc/>.
- [58] P. Reu, Introduction to digital image correlation: Best practices and applications, *Exp. Tech.* **36**, 3 (2012).
- [59] J. Main, S. Peterson, and A. Strauss, Load-deflection behavior of space-based inflatable fabric beams, *J. Aerosp. Eng.* **7**, 225 (1994).
- [60] R. Comer and S. Levy, Deflections of an inflated circular-cylindrical cantilever beam, *AIAA J.* **1**, 1652 (1963).
- [61] E. N. Antoine, Prestressed concrete analysis and design, Fundamentals, USA, 1 (2004).
- [62] N. Arthur, Nilson Arthur H, (1987) “design of prestressed concrete (1987)”.
- [63] E. G. Nawy, Reinforced concrete, A Fundamental Approach (1996).
- [64] R. I. Gilbert and N. C. Mickleborough, *Design of Prestressed Concrete* (CRC Press, London EC4P 4EE, England, 1990).
- [65] J. F. Labuz and A. Zang, in *The ISRM Suggested Methods for Rock Characterization, Testing and Monitoring: 2007-2014* (Springer, Gewerbestrasse 11, 6330 Cham, Switzerland, 2012), p. 227.
- [66] J. Atkinson, *An Introduction to the Mechanics of Soils and Foundations: Through Critical State Soil Mechanics* (McGraw-Hill Book Company (UK) Ltd, Oxfordshire, UK, 1993).
- [67] A. R. Jumikis, Mechanics of soils, *Soil. Sci.* **98**, 278 (1964).
- [68] I. Smith, *Smith’s Elements of Soil Mechanics* (John Wiley & Sons, West Sussex, PO19 8SQ, UK, 2014).
- [69] M. Budhu, *Soil Mechanics Fundamentals* (John Wiley & Sons, West Sussex, PO19 8SQ, UK, 2015).
- [70] P. V. Lade, *Triaxial Testing of Soils* (John Wiley & Sons, West Sussex, PO19 8SQ, UK, 2016).
- [71] R. H. Parry, *Mohr Circles, Stress Paths and Geotechnics* (CRC Press, London, UK, 2004).
- [72] R. Zalewski, P. Chodkiewicz, and M. Shillor, Vibrations of a mass-spring system using a granular-material damper, *Appl. Math. Model.* **40**, 8033 (2016).
- [73] G. Johnson and W. Cook, in *Seventh International Symposium on Ballistics, the Hague, the Netherlands*, Vol. 21 (1983), p. 541.
- [74] W. Cen, J. R. Luo, W. D. Zhang, and M. S. Rahman, An enhanced generalized plasticity model for coarse granular material considering particle breakage, *Adv. Civ. Eng.* **2018**, 1 (2018).
- [75] A. Wosatko, A. Winnicki, M. A. Polak, and J. Pamin, Role of dilatancy angle in plasticity-based models of concrete, *Arch. Civ. Mech. Eng.* **19**, 1268 (2019).